REVISION 1

Crystal structure, hydrogen bonding and high-pressure behavior of the hydroxide perovskite MgSi(OH)$_6$: a phase relevant to deep subduction of hydrated oceanic crust.

Mark D. Welch[1], Jens Najorka[1] and Bernd Wunder[2]

[1]Natural History Museum, London SW7 5BD, United Kingdom.

[2] Deutsches GeoForschungsZentrum GFZ, Section 3.6, Telegrafenberg, 14473 Potsdam, Germany.

Abstract

The structural response to compression of the synthetic high-pressure hydroxide perovskite MgSi(OH)$_6$, the so-called "3.65 Å phase", has been determined to 8.4 GPa at room temperature using single-crystal XRD in the diamond-anvil cell. Two very similar structures have been determined in space groups $P2_1$ and $P2_1/n$, for which differences in oxygen donor-acceptor distances indicate that the non-centrosymmetric structure is likely the correct one. This structure has six non-equivalent H sites, of which two are fully occupied and four are half-occupied. Half-occupied sites are associated with a well-defined crankshaft of hydrogen-bonded donor-acceptor oxygens extending parallel to c. Half occupancy of these sites arises from the averaging of two orientations of the crankshaft H atoms ($\parallel \pm c$) in equal proportions. The $P2_1$ and $P2_1/n$ structures are compared. It is shown that the former is likely the correct space group, which is also consistent with recent spectroscopic studies which recognize six non-equivalent O-H. The structure of MgSi(OH)$_6$ at pressures up to 8.4 GPa was refined in both space groups to see how divergent the two models are. There is a very close correspondence between the responses of the two structures implying that, at least to 8.4 GPa, non-centrosymmetry does not affect compressional behaviour. The very different

compressional behavior of MgO_6 and SiO_6 octahedra observed in this study suggests that structural phase transformations or discontinuities likely occur in $MgSi(OH)_6$ above 9 GPa.

Introduction

Hydroxide perovskites of general stoichiometry $BB'(OH)_6$ are frameworks in which adjacent corner-linked octahedra are occupied by heterovalent or homovalent cations, e.g. $CaSn(OH)_6$, $NaSb(OH)_6$, $FeGe(OH)_6$, $Fe(OH)_3$, $Ga(OH)_3$, $In(OH)_3$. The large cavity in which the A-site of the normal perovskite structure lies is empty. All oxygen atoms form O-H groups and there is extensive hydrogen bonding. The combination of an empty A site and strong hydrogen bonding leads to a highly rotated framework. The crystal chemistry of hydroxide perovskites is reviewed by Mitchell et al. (2017).

Basciano et al. (1998) used neutron powder diffraction to study the cubic hydroxide perovskite schönfliesite $MgSn(OH)_6$ and showed that each oxygen atom is both a donor and acceptor of a hydrogen bond, and that both non-equivalent H sites are half-occupied. Using single-crystal XRD, Lafuente et al. (2015) located all four half-occupied H sites (and single full H site) of tetrawickmanite $MnSn(OH)_6$. We have since located H atoms in stottite $FeGe(OH)_6$, schönfliesite, wickmanite, tetrawickmanite and söhngeite $Ga(OH)_3$ by single-crystal XRD, e.g. Welch and Kleppe, 2016. The cubic phases schoenfliesite, burtite $CaSn(OH)_6$, vismirnovite $ZnSn(OH)_6$, dzahlindite $In(OH)_3$ and wickmanite have isolated rings of four O-H…O linkages in which each of the two non-equivalent H sites is half-occupied as in schönfliesite. Tetragonal phases such as stottite (SG $P4_2/n$) and tetrawickmanite (SG $P4_2/n$) have ...O-H…O-H…O-H… donor-acceptor crankshafts and isolated four-membered rings. Each of the four non-equivalent crankshaft H sites is half-occupied and the ring H site is full. Half-occupancy of H sites arises from an averaging of

two different identical orientations of the hydrogen-bonding configuration of the donor-acceptor crankshaft, as we discuss in this paper with regard to $MgSi(OH)_6$.

MgSi(OH)$_6$ hydroxide perovskite
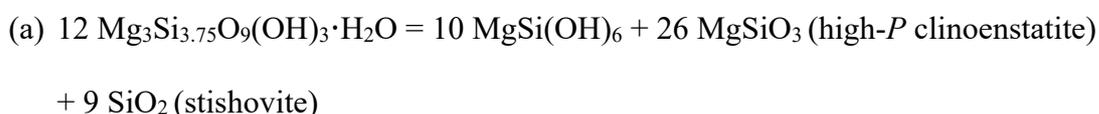
The synthetic hydroxide perovskite $MgSi(OH)_6$ is now known to be of geophysical significance as one of a sequence of high-pressure hydrous phases which experiments indicate as having key roles in the transport of H_2O into the deep mantle, e.g. Mookherjee et al. (2015), Rashchenko et al. (2016), Koch-Müller et al. (2021). This phase was first synthesized by Sclar et al. (1965) who referred to it as the "3.65Å-phase", the name referencing a characteristic strong Bragg reflection in the powder diffraction pattern. The structure of the 3.65Å-phase remained unknown until Wunder et al. (2011) published a provisional structure based upon a close similarity of the powder-diffraction pattern to that of δ-Al(OH)$_3$ (Matsui et al. 2011); the structure was inferred to be a perovskite-like framework of corner-linked *B*-octahedra but lacking the *A*-site cation characteristic of perovskites. The provisional structure proposed by Wunder et al. (2011) had Mg and Si disordered at a single cation site, a very unlikely scenario in view of the very different bond-valences of Mg-O and Si-O, with the formation of Si-O(H)-Si bridges being implied for a disordered structure. A more crystallographically reasonable structure would consist of alternating MgO_6 and SiO_6 octahedra, as was found subsequently by Welch and Wunder (2012) in monoclinic space group $P2_1/n$. In this paper we refer to the 3.65Å-phase as $MgSi(OH)_6$.
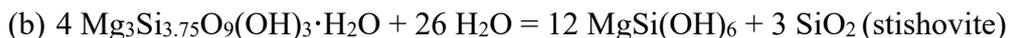
Recent high-PT experiments have shown that $MgSi(OH)_6$ is formed by the decomposition of the superhydrous sheet silicate 10Å-phase at ~10 GPa (Rashchenko et al. 2016). 10Å-phase forms from talc at 4-5 GPa, 500-700 °C (Pawley et al. 2011). Welch et al. (2006) discovered how talc transforms to 10Å-phase by the formation of vacancies in the tetrahedral sheet via the substitution $^{IV}SiO_4 \rightarrow (OH)_4 + ^{IV}\otimes$ ($\otimes$ = vacant Si site). Their sample

of 10Å-phase, synthesized at 6.5 GPa/450 °C (12 hr), had an analysed composition (minus H) of $Mg_3Si_{3.83(8)}O_{13.1(4)}$ and an implied corresponding average formula (for 0.17 $H_4\otimes_1Si_{-1}$ substitution) of $Mg_3Si_{3.83(8)}O_{9.32}(OH)_{2.68}\cdot1.1(4)$ H_2O, i.e. 4% $^{IV}\otimes$. Previous studies had not identified the presence of Si vacancies. Their presence is of fundamental importance as it transforms the hydrophobic sheet of tetrahedra of talc into a hydrophilic sheet by protonation and thereby furnishes hydroxyl groups that can form hydrogen bonds with oxygen atoms of interlayer H_2O molecules. The incorporation of interlayer H_2O is not possible for talc without the formation of Si vacancies.

Critically, the formation of Si vacancies, even in low proportions, increases the in-plane compressibility of the 2:1 sheet, resulting in a smaller unit cell volume overall, even with interlayer hydration. Hence, such a mechanism of hydration with densification explains the much higher baric stability of 10Å-phase compared with talc. Prior to the identification and recognition of the role of Si vacancies in 10Å-phase, an explanation for the transformation from talc was elusive.

Several studies have shown that talc transforms to the 10Å-phase in a few hours at 4-6 GPa/500-600 °C (Welch et al., 2006; Phillips et al., 2007; Rashchenko et al., 2016). Hence, there appears to be no significant kinetic barrier to the formation of 10Å-phase, i.e. it is to be expected that talc will transform to 10Å-phase in cold subduction zones. The geological significance of the 10Å-phase is that it acts as a bridge for the transfer of H_2O into the deep mantle from the crustal components of a subducting slab where talc occurs to transition-zone depths where $MgSi(OH)_6$ is stable, i.e. talc → 10Å-phase → $MgSi(OH)_6$. For example, consider 10Å-phase of composition $Mg_3Si_{3.75}O_9(OH)_3\cdot H_2O$ (⟹ 6% $^{IV}\otimes$). Two different reactions can occur depending upon whether free H_2O is a reactant or not:

(a) 12 $Mg_3Si_{3.75}O_9(OH)_3\cdot H_2O$ = 10 $MgSi(OH)_6$ + 26 $MgSiO_3$ (high-P clinoenstatite)

   + 9 SiO_2 (stishovite)

(b) 4 $Mg_3Si_{3.75}O_9(OH)_3\cdot H_2O$ + 26 H_2O = 12 $MgSi(OH)_6$ + 3 SiO_2 (stishovite)

The reaction 10Å-phase + $H_2O \rightarrow MgSi(OH)_6$ + stishovite has been located from high-PT experiments by Rashchenko et al. (2016) at 10 GPa (up to 450 °C). Their study indicated that $MgSi(OH)_6$ is stable to at least 500 °C at 12 GPa. The dehydration reaction $MgSi(OH)_6 \rightarrow$ high-P clinoenstatite + H_2O has a positive dP/dT, implying that $MgSi(OH)_6$ is likely stable to $P > 14$ GPa and $T > 550$ °C.

Geotherms associated with the crustal component of cold subduction, of the order of 1-3°/km (Syracuse et al. 2010; Rashchenko et al. 2016), lie well within the stability field of $MgSi(OH)_6$ determined thus far. The ultra-high-P stability (>12 GPa) of this phase remains to be determined, and it is conceivable that it is stable at P-T conditions of the lower mantle in cold subduction zones.

The equations-of-state of several hydroxide perovskites have been reported, all but one of which have bulk moduli K_0 of 70-80 GPa (Ross et al. 2002; Mookherjee et al. 2015; Najorka et al. 2019). The exception is burtite $CaSn(OH)_6$, which has an exceptionally low bulk modulus of 42 GPa (Welch and Crichton, 2002). No studies of the detailed structural pressure responses of hydroxide perovskites have been made and the compression mechanisms involved are unknown.

Mookherjee et al. (2015) studied the compression of $MgSi(OH)_6$ to 41 GPa, and, using powder X-ray diffraction, derived a bulk modulus from a fit to a 3rd-order Birch-Murnaghan equation-of-state of 83 ±1 GPa (K_0' of 4.9 ±0.2). $MgSi(OH)_6$ remained crystalline at the highest pressure studied (41 GPa) and can be recovered reversibly on decompression to room pressure. No structural data were determined other than unit-cell parameters using the Le Bail method.

Basu et al (2022) reported the results of a Raman spectroscopic study of $MgSi(OH)_6$ to 60 GPa in which they recognized six different O-H bands comprising a quartet (Raman

shifts of 3144–3288 cm^{-1}) and a pair (3403 and 3459 cm^{-1}). The Raman shifts of all bands

decrease with increasing pressure, indicating an increase in the strength of hydrogen bonding

on compression. Furthermore, all Raman bands broadened significantly with increasing

pressure, suggesting proton disorder.

All hydroxide perovskites have highly rotated octahedra, due to framework collapse

around the vacant A site coupled with strong hydrogen bonding that leads to short donor-

acceptor O(-H)…O distances, e.g. <2.8 Å. All have very similar degrees of rotation of

octahedra (14-17º), although they adopt a variety of octahedral tilt systems (Mitchell et al.

2017). MgSi(OH)$_6$ provides an opportunity to follow the compressional behavior of a

structure having two very different octahedra that are expected to respond differently to

compression.

In this paper we present new structural data for MgSi(OH)$_6$ for which it has been

possible to locate all H atoms of the structure, thereby identifying the hydrogen-bonding

network for the first time. We have determined the structure in space groups $P2_1/n$

(centrosymmetric) and $P2_1$ (non-centrosymmetric) and compare these two closely related

models and their high-pressure responses. We report the $P2_1/n$ structure as this provides a

basis for considering the derivation of the very similar $P2_1$ structure, which we show is likely

the correct one. The high-pressure behaviour of MgSi(OH)$_6$ is modelled using both structures

and the results are compared.

The topology of MgSi(OH)$_6$ is shown in Figure 1. It consists of a framework of highly

rotated MgO$_6$ and SiO$_6$ octahedra in which all oxygen atoms form OH groups. The hydrogen

bonding topology comprises O(H)…O(H) crankshafts and zigzag chains extending $\|c$ and

$\|[010]$, respectively, as is described in detail below. The $P2_1/n$ topology has tilt system $a^-a^-c^+$

(Howard et al. 2003) with axes related to those of the cubic aristotype ($Pm\overline{3}m$) by (1,1,0 $\overline{1}$,1,0

0,0,2); $P2_1$ has the same tilt system. The $P2_1/n$ topology is very common in perovskites

sensuo strictu having a 1:1 B-cation ratio and ordered on the "rock-salt" pattern (e.g. Barnes et al. 2006).

Experimental Methods

Data collection

Several crystals of $MgSi(OH)_6$ were examined from a product synthesised by Wunder et al. (2011) at 10 GPa and 450ºC from a gel of composition $MgO \cdot SiO_2$ with excess water. A high-quality tabular $MgSi(OH)_6$ crystal ("crystal 6") having dimensions $35 \times 90 \times 90$ μm was suitable for the high-P study. This crystal was characterised under ambient conditions outside the diamond-anvil cell before and after the high-P experiments. A second, larger crystal ("crystal 7") $55 \times 120 \times 140$ μm was used to obtain data at 100K. This crystal is too large and has an unsuitable shape for the diamond anvil cell (DAC) but allowed all ten H atoms of the $P2_1$ structure to be located.

Single-crystal X-ray diffraction experiments were carried out under ambient and high-P conditions using a Xcalibur-E four-circle diffractometer (Rigaku Oxford Diffraction) equipped with a graphite monochromator and an EoS area detector. Graphite-monochromatized Mo$K\alpha$ radiation was used at 50 kV and 40 mA. The sample-to-detector distance was 68 mm. Data were collected using omega scans up to 35 ºθ.

For measurements of the two crystals at 100K and 293K, the scan width and frametime used were 1º and 120-180 s, respectively. High-P data experiments on crystal 6 used a scan width of 0.75º and collection times of 120-170 s. Coverage of the reflection sphere for high-P data collections was 31-32%, a consequence of the spatial limitations imposed by the DAC. Image frames from high-P datasets were examined to check for interference between crystal and diamond reflections; those with poor merging, caused by

reflection clipping (gasket shadowing) at high-θ or interference with diamond were examined using CrysalisPro. High-θ frames were checked and suspect reflections noted and later removed from *hkl* lists. The mounting orientation of the pair of diamonds produced very few reflections, so that interference with sample reflections was rare; typically, fewer than 10 reflections were excluded.

A Cryostream cryojet (Oxford Instruments) with liquid nitrogen source was used for the 100 K experiment on crystal 7. The crystal was glued with epoxy to a 100 μm diameter rigid mylar loop and cooled to 100 K at a rate of 6 K/min. The inner-sheath stream of the Cryostream delivers a laminar flow to the crystal with a cross-section of about 400 μm at a nozzle-to-crystal distance of 7 mm; an outer stream of nitrogen gas ensures that laminar flow occurs without turbulence and consequent icing.

After the ambient experiment, crystal 6 was loaded into a four-post Mao-Bell DAC (Diamond Optics, Tucson, Arizona, USA) for the high-*P* study. Pressure was applied by tightening four screws by hand. Diamonds with an opening angle of 70º were used and fitted with tungsten carbide backing seats of Boehler-Almax design. The diamonds had a culet diameter of 600 μm. A tungsten gasket (thickness 250 μm) was pre-indented to a depth of 75 μm and a hole of 200 μm diameter drilled using a spark eroder. The tabular crystal was placed on the culet with its largest flat face (110) lying parallel to the culet surface and being 35 μm thick parallel to the DAC axis. A ruby sphere (20 μm diameter) was placed near the $MgSi(OH)_6$ crystal for pressure calibration using the ruby-fluorescence method (Mao et al., 1986). Ruby fluorescence was measured using an Ocean Optics device equipped with a diffraction grating and green laser light (532 nm). The pressures reported here are for the ruby R1 line and were obtained by fitting Lorentzian curves to R1 and R2 lines. Pressures were measured before and after each high-*P* experiment. The *P*-transmitting medium was a

methanol-ethanol mixture in 4:1 ratio, which allows hydrostatic conditions during the experiments up to 9.8 GPa (Angel et al 2007).

High-P XRD data were collected at 0.71, 2.76, 4.73, 6.22, 7.23, 8.40 and 9.11 GPa on compression, and at 4.84 and 3.53 GPa on decompression. Reflection intensities were corrected for Lorentz-polarisation effects using CrysAlisPro (Rigaku Oxford Diffraction). For 100K and 293K datasets collected outside the DAC an empirical multiscan absorption correction using ABSPACK (2017) was applied. For high-pressure datasets a numerical absorption correction (based upon crystal shape, size and location on culet) was applied using Absorb v7 (Angel and Gonzalez-Platas, 2013); this method produced corrected reflection intensities and merging values very similar to those obtained from the multiscan correction using ABSPACK. The low R_{int} values for all datasets (0.023-0.038) are consistent with a high-quality crystal and reliable corrected intensities. The use of a W gasket minimized problems with interference from powder-diffraction rings of WC; rings were at near-background levels and so it was not considered necessary to correct intensities for them.

Crystal structure refinements

The structures of crystals 6 and 7 were refined using SHELX version 2018/3 (Sheldrick, 2015) within the WinGX suite of programs (Farrugia 1999). Neutral atomic scattering factors (Wilson, 1992) were used. Refinements were carried out in space groups $P2_1/n$ and $P2_1$, as both have been reported previously. For refinement of the $P2_1/n$ structure the model determined by Welch and Wunder (2012), which did not include H atom positions, was used as a starting point. The $P2_1$ structure was solved by direct methods (SHELX) as described below. Ambient structures of crystal 6 outside the DAC were obtained before and

after the high-P experiment. The ambient structure obtained before the experiment was used as the starting model for refinement of high-P structures.

Images of crystal structure presented in this paper were generated using CrystalMaker® (CrystalMaker Software Ltd, Oxford, England, www.crystalmaker.com). Polyhedral parameter calculations based upon Robinson et al. (1971) used VESTA3 (Momma and Izumi, 2019).

Results

Previous studies have indicated space groups $P2_1/n$ and $P2_1$ as possible for $MgSi(OH)_6$. We have refined its structure in both space groups to allow a comparison and so choose the most likely space group. As noted above, the recent paper by Basu et al. (2022) using Raman spectroscopy recognized six O-H bands, this being consistent with $P2_1$ symmetry.

Welch and Wunder (2012) reported that refinement in $P2_1$ was problematic. In part, this may have been due to using 30°θ as the diffraction limit and 50 s frametime. We have used a longer frametime (170 s) and collected to 35°θ, with the expectation that increased resolution and number of reflections with $I > 2\sigma(I)$ would allow precise location of H atoms and the detection of subtle structural differences (interatomic distances) indicative of a non-centrosymmetric structure ($P2_1$).

Here, we first report refinements of the structure at 100 K and 293 K in space groups $P2_1/n$ and $P2_1$ for crystals 6 and 7. We then describe the refinements of the high-P structures for crystal 6. As we explain below, for the high-P data it was only possible to obtain isotropic refinements for the $P2_1$ structure, and so for the purposes

of direct comparison refinements of the high-P structure in space group $P2_1/n$ were also isotropic.

The identification of plausible H sites was based upon O-H bond distances (i.e. 0.8-0.9 Å for XRD) and O(-H)….O donor-acceptor distances from the list of unmodeled electron-density maxima in the difference-Fourier map (SHELXL "Q-peak" list). A soft constraint of 0.85 ± 0.03 Å for O-H bonds was used in refinements, which recognises that hydroxyl bond-lengths determined by X-ray diffraction are much shorter than the true values, due to displacement of the H electron towards the oxygen donor atom. Unsurprisingly, H atoms were not found in the high-P refinements.

Table 1 (deposit item) summarizes the results of the 100K refinement in space group $P2_1$. Atom coordinates and displacement parameters for 100K structures of crystal 7 in space groups $P2_1/n$ and $P2_1$ are shown in Table 2 (deposit item). Bond lengths and polyhedral parameters for both structures are shown in Table 3. Refinements of crystal 6 at 293K for both space groups are deposited as CIF files.

$P2_1/n$ refinements

For the 100K and 293K refinement of crystals 6 and 7, all five H atoms of the $P2_1/n$ structure appeared in the difference-Fourier map after five cycles of isotropic least-squares refinement without reflection weighting: the highest residuum (0.9 e/Å^3) is a fully occupied H site (H2); Four smaller residua ($0.47-0.65$ e/Å^3) correspond to half occupied H sites (H1, H3, H4, H5). All five H atoms were included in the structural model and their positions and an overall U_{iso} refined with reflection weighting applied. The structure is described below and is almost identical to that reported by Welch and Wunder (2012), except that all five non-equivalent H atoms have now been recognized and located (Table 2, deposited).

P2₁ refinements

The non-centrosymmetric structure of $MgSi(OH)_6$ is pseudo-centrosymmetric and has space group $P2_1$. The structure refinements of crystals 6 and 7 at ambient conditions reflect this character in having inconclusive values for their Flack parameters. There are also numerous high correlations between the coordinates (and U_{ij}) of oxygen atoms related by a centre of symmetry. The 100 K structure refinement of crystal 7 has values of 0.0(5) and 0.0(4) for conventional Flack and Parsons' Flack parameters (Flack and Bernardinelli 1999; Parsons et al. 2012), respectively, both of which suggest, albeit with large uncertainties, that the correct absolute structure was determined. Below, we present structural details that indicate $P2_1$ symmetry. Similarly, the refinement of crystal 6 (293 K) gave Flack (conventional) = 0.5(7) and Flack (Parsons) = 0.3(3); as such, the absolute structure could not be determined conclusively.

The structure of crystal 7 at 100 K was solved in SG $P2_1$ by direct methods using SHELXS (Sheldrick, 2015). Mg, Si and all six non-equivalent oxygen atoms were found. Ten structurally plausible H sites were identified based upon O-H bond lengths and O(-H)….O donor-acceptor distances from the list of unmodeled electron-density maxima in the difference-Fourier map obtained after an initial 5 cycles of least-squares isotropic refinement without reflection weighting; the list of maxima as output by SHELX is shown in Figure 2 (deposited with the journal). Two of these maxima (1.00 and 0.97 e/Å³) correspond to fully-occupied H sites of the two zigzag chains; the other eight maxima (0.47 – 0.75 e/Å³) correspond to partially-occupied sites of the crankshaft. For refinement, all ten maxima were assigned to H and modeled as two sites with full occupancy (H1 and H2) and eight with half occupancy (H3 to H10); an overall U_{iso} for H atoms and a soft bond-length restraint on O-H bonds (see above) were applied. Refinement of the positions of all H atoms proceeded smoothly. The results of the refinement of the 100 K $P2_1$ structure are given in Tables 1-3.

CIFs for the $P2_1$ refinements of crystal 7 at 100 K and 293 K are available as Supplementary Material documents xtl7_P21_100K.CIF and xtl7_P21_293K.CIF, respectively.

In the $P2_1$ structure the two non-equivalent zig-zag chains, O1(H1)…O1(H1) and O2(H2)…O2(H2), which are equivalent in $P2_1/n$ (related by a center of symmetry), have $d(O_D…O_A)$ values of 2.949(2)Å and 2.955(2)Å, respectively; these values are comparable to the O2(H2)…O2(H2) distance (2.952Å) of the $P2_1/n$ structure. The eight half-occupied H sites of the crankshaft have a configuration that is very similar to that of the crankshaft of the $P2_1/n$ structure. The crankshafts of these two structures are compared in Figure 3. Donor-acceptor distances, H…O_A distances and O_D-H…O_A angles are shown in Table 3. Bearing in mind that H positions were restrained and that O-H distances determined by X-ray diffraction are at least 0.1 Å shorter than true values, we include H…O_A distances and O_D-H…O_A angles as a general indication of the strength and directionality of hydrogen bonds. The high directionality (high O_D-H….O_A angles) and short lengths of hydrogen bonds in the structure indicate strong hydrogen bonding. There is no evidence for birfurcated hydrogen bonds.

Geometrical parameters of MgO_6 and SiO_6 octahedra for $P2_1/n$ and $P2_1$ structures are shown in Table 3. These parameters for isotropic and anisotropic refinements of the $P2_1$ structure are almost identical. The refinement of the 293K structure of crystal 7 is substantially the same as that obtained for 100K. Again, all ten H atoms appeared in the first few cycles of isotropic least-squares without weighting.

Comparison of $P2_1$ and $P2_1/n$ structures

Both structures have crankshafts in which all H sites are half-occupied. In $P2_1/n$, half-occupancy of H1a and H3a sites is required by the location of centers of symmetry, whereas H1b and H3b sites are, in principle, free to have variable occupancy. In the $P2_1/n$ structure at

293K the zigzag chain has d(O2…O2) of 2.943(3)Å; in $P2_1$ the two corresponding

distances d(O1…O1) and d(O2…O2) are 2.946(4)Å and 2.957(4)Å, respectively.

The clearest indication that $P2_1$ symmetry is likely the correct choice over $P2_1/n$ is

given by the values of d(O3…O6) and d(O4…O5) of the crankshaft in the 100K $P2_1$

structure, which are 2.814(3)Å and 2.772(3)Å, respectively (Fig. 3). The difference between

the two non-equivalent distances in the $P2_1$ structure (0.04Å at 100K, 0.03Å at 293K) is not

trivial. Geometrical parameters of MgO_6 and SiO_6 octahedra for the two structures are almost

identical; polyhedral volumes are the same (Table 3).

High-pressure behaviour

Here, we report the high-P behaviour of $MgSi(OH)_6$ as modelled by $P2_1/n$ and $P2_1$

structures for crystal 6. Out-of-cell refinements of crystal 6 at 293K before and after the high-

P experiment are deposited as CIFs xtl6_ P21_293K_amb_before.CIF and

xtl6_P21_293K_amb_after.CIF. The smaller number of unique data obtained in the high-P

experiments relative to the out-of-cell collections, due to the geometrical limits imposed by

the DAC, did not allow stable anisotropic refinement in space group $P2_1$ at any pressure.

Consequently, an isotropic model (without H atoms) was used for refinements of all $P2_1/n$

and $P2_1$ structures.

Unit-cell parameters at various pressures at 293K are shown in Table 4 and the results

of refinements are summarized in Table 5. The variation of normalised unit-cell parameters

and unit-cell volume with pressure are shown in Figures 4a and 4b, respectively. As this

study focussed on the details of crystal structure rather than the derivation of high-quality

bulk and axial moduli (a different diffractometer configuration would be needed to achieve

this), approximate values of the bulk modulus and axial moduli of $MgSi(OH)_6$ were obtained

by fitting a 2nd-order Birch-Murnaghan equation-of-state to the compression data using the program *EOSFIT* version 7c (Angel et al., 2014). The values of bulk and axial moduli obtained are: $K_0 = 80.3(9)$ GPa, $K_{a0} = 68.2(8)$ GPa, $K_{b0} = 85.1(9)$ GPa, $K_{c0} = 89.4(7)$ GPa (K' fixed at 4 for all); fits to the data using these values are shown in Figure 4. The compression curves for *b*- and *c*-parameters are very similar, whereas that for the *a*-parameter lies well below these trends and implies a higher compressibility of the structure in this direction.

Examination of the successful anisotropic refinements for space $P2_1/n$ showed that displacement ellipsoids had reasonable shapes and sizes that are comparable to those of the ambient out-of-cell structure, with no indication of absorption problems. An example showing the form of displacement ellipsoids is shown in Figure 5 for anisotropic refinement of the 6.2 GPa dataset (CIF deposited as document x6_6p2GPa_ANIS.cif), from which it is evident that there are no anomalous effects that could imply a problematic absorption correction.

Variations with pressure of Mg-O and Si-O bond distances, oxygen donor-acceptor hydrogen-bonded distances $d(O_D...O_A)$ and Mg-O-Si bond angles for both structure models are shown in Figures 6, 7 and 8. Variations with pressure of polyhedral parameters for both structures are shown in Figure 9.

$P2_1/n$ model at high P

The ambient $P2_1/n$ structure obtained before the high-*P* experiment was used as the initial model for the refinement of high-*P* structures. H atoms could not be located for high-*P* structures. Nonetheless, knowing the hydrogen-bonding topology of the ambient structure provides a sound basis for interpreting high-*P* structures, as $O_D...O_A$ distances are easily identified and quantified.

Some high-P structures of $MgSi(OH)_6$ could be refined anisotropically. In other cases, anisotropic refinement led to non-positive-definite values for U_{ij} of the O1 atom. For consistency, therefore, we have chosen to present only isotropic refinements.

Trends of Mg-O and Si-O bond lengths with pressure to 9.2 GPa for the $P2_1/n$ structure (Fig. 6a,c) are smooth, with no hint of discontinuity. Figure 7 shows (only as dotted lines for $P2_1/n$) that all four $d(O_D...O_A)$ distances of the $P2_1/n$ structure decrease smoothly on compression. The trends are nearly parallel, except for convergence of $d(O1_D...O1_A)$ and $d(O3_D...O3_A)$ of the crankshaft. Trends of the three independent Mg-O-Si angles also vary smoothly and have parallel trends (Fig. 8).

Geometrical variations with pressure of MgO_6 and SiO_6 octahedra are shown in Figure 9. The polyhedral volume of the SiO_6 octahedron decreases linearly, whereas that of the MgO_6 octahedron is clearly non-linear and may be composed of two segments with a kink between 5 and 6 GPa. Polyhedral parameters of the two structures determined before and after the high-P experiment are summarized in Table 7 from which it is evident that before/after values are almost identical. Furthermore, structural parameters obtained at 3.5 GPa and 4.8 GPa on decompression lie on the trends defined by those obtained on compression, most clearly seen for the 4.8 GPa structure. Hence, the high-pressure response of $MgSi(OH)_6$ to 9 GPa is fully reversible and without detectable hysteresis.

$P2_1$ model at high P

All attempts to refine the high-pressure data for the $P2_1$ structure anisotropically resulted in at least three of the six non-equivalent oxygen atoms having non-positive-definite U_{ij} values. Consequently, the isotropic ambient structure was used as the model for refining high-P structures.

Trends of Mg-O and Si-O bond lengths with pressure for the $P2_1$ structure (Fig. 6b,d) are more variable than their $P2_1/n$ counterparts, although they generally follow the trends of the latter. The greater freedom to distort (absence of a center of symmetry) results in more variation in bond lengths for the $P2_1$ structure.

The variation of $O_D...O_A$ distances of the $P2_1$ structure with pressure are shown in Figure 7. The four crankshaft distances follow similar trends. The $O_D...O_A$ distances of the two zig-zag $O(H)...O(H)$ chains extending parallel to [010] are similar to each other. In all cases trends in $d(O_D...O_A)$ mirror those of the $P2_1/n$ structure (shown as dotted lines in Fig. 7). As is the case for the $P2_1/n$ structure, $d(O_D...O_A)$ values determined for the two pressures on decompression are very similar to those obtained on compression. Mg-O-Si angles (Fig. 8) decrease systematically with increasing pressure; $P2_1/n$ trends are shown as dotted lines and, in general, correlate with those of the $P2_1$ structure. The values of polyhedral volumes at high pressure for the $P2_1/n$ and $P2_1$ models are almost congruent (Fig. 9). Polyhedral parameters for the before/after $P2_1$ structures (Table 7) are almost identical and are also very similar to those of the before/after $P2_1/n$ structures.

Discussion and Implications

Structure refinements in space groups $P2_1/n$ and $P2_1$ are very similar for both 100K and 293K datasets. However, the clear non-equivalence of two crankshaft $O_D...O_A$ distances (2.79Å and 2.82Å) in the $P2_1$ structure that are equivalent in $P2_1/n$ (related by a center of symmetry) is good evidence for the non-centrosymmetric space group being the correct choice. Refinement in space group $P2_1$ indicates that small displacements of oxygen atoms occur relative to the $P2_1/n$ structure. We note that Mg-O and Si-O bonds of the refined $P2_1$ structure are much longer than those modeled using Density Functional Theory by Wunder et al.

(2012) for this space group. As a consequence, the volumes of MgO_6 and SiO_6 octahedra obtained by DFT ($11.41Å^3$ and $7.49Å^3$) are much smaller than those determined experimentally ($12.15Å^3$ and $7.67Å^3$).

The recent study of $MgSi(OH)_6$ by Basu et al. (2022) using Raman spectroscopy to 60 GPa is consistent with $P2_1$ symmetry and the structure determined here. Longer $O_D…O_A$ distances correlate with weaker hydrogen bonding and higher vibrational frequencies of O-H bonds (e.g. Libowitzsky, 1999). On this basis, the four non-equivalent $O_D…O_A$ distances of the crankshaft correspond to four of the six OH Raman bands as follows: OH-3/O4…O6, OH-4/O3…O5, OH-6/O4…O5, OH-5/O3…O6. The two non-equivalent O of the zigzag chains correspond to the pair of Raman bands as follows: O-H1/O1…O1 and O-H2/O2…O2. Thus, there is now convergent independent structural and spectroscopic data that support $P2_1$ as the correct space group for $MgSi(OH)_6$. The axial moduli obtained in the present study also indicate a clear anisotropic response of the structure that correlates with the different hydrogen bonding connectivity along principal directions of the unit cell.

It is clear why space group $P2_1/n$ mimics the $P2_1$ structure so closely: the latter has an averaged H-bonding network comprising two almost identical orientations directed along $+c$ and $-c$. The close similarity of the two sets of four H atoms of the $P2_1$ crankshaft is very closely approximated by the $P2_1/n$ structure. The significance of the dual orientation of the hydrogen-bonded network of the crankshaft remains to be determined. The $P2_1$ and $P2_1/n$ models give almost identical trends of structural parameters with P. Thus, it can be concluded that to 8.4 GPa the lower symmetry of $P2_1$ does not lead to different structural behavior relative to $P2_1/n$, and that there are no signs of a structural phase transition.

The acknowledged relevance of $MgSi(OH)_6$ to understanding the hosting and distribution of water in the deep mantle within the context of cold subduction means that

crystallographic and spectroscopic studies of its behavior at high pressure and temperature are likely to provide significant insights into its role as a water-carrier. The present study has provided the first detailed structural characterization of this phase, including an initial study of its high-pressure behavior. This information, coupled to spectroscopic observations, is essential for evaluating future studies of $MgSi(OH)_6$ at high P and T within its stability range. The very different responses to compression of the MgO_6 and SiO_6 octahedra are a potential source of discontinuous behavior at pressures higher than those investigated here.

Acknowledgments

References

ABSPACK S (2017) A Rigaku Oxford Diffraction program for Absorption Corrections

Angel, R.J., Gonzalez-Platas, J. (2013) ABSORB-7 and ABSORB-GUI for single-crystal absorption corrections. Journal of Applied Crystallography, 46, 252-254.

Angel, R.J. and Gonzalez-Platas, J. and Alvaro, M. (2014) Eosfit-7c and a Fortran module (library) for equation of state calculations. Zeitschrift für Kristallographie, 229, 405-419.

Barnes, P.W., Lufaso, M.W. and Woodward, P.M. (2006) Structure determination of $A_2M^{3+}TaO_6$ and $A_2M^{3+}NbO_6$ ordered perovskites: octahedral tilting and pseudosymmetry. Acta Crystallographica, B62, 384-396.

Basciano, L.C., Peterson, R.C., Roeder, P.L. and Swainson, I. (1998) Description of schoenfliesite, $MgSn(OH)_6$, and roxbyite, $Cu_{1.72}S$, from a 1375 BC shipwreck, and Rietveld neutron-diffraction refeinement of synthetic schoenfliesite, wickmanite, $MnSn(OH)_6$, and burtite $CaSn(OH)_6$. Canadian Mineralogist, 36, 1203-1210.

Basu, A., Mookherjee, M., Bucag, C., Tkachev, S. and Wunder, B. (2022) High-pressure behavior of 3.65 Å phase: Insights from Raman spectroscopy. American Mineralogist (in press).

Flack, H.D. and Bernardinelli, G. (1999) Absolute structure and absolute configuration. Acta Crystallogr. Sect. A 55, 908–915.

Farrugia, L. J. (1999) WinGX: An integrated system of Windows Programs for the solution, refinement and analysis of single-crystal X-ray diffraction data. Journal of Applied Crystallography, 32, 837–838.

Koch-Müller, M., Appelt, O., Wunder, B. and Wirth, R. (2021) New insights in the mechanisms of the reaction 3.65Å phase = clinoenstatite + water down to nanoscales. European Journal of Mineralogy, 33, 675-686.

Lafuente, B., Yang, H. and Downs, R.T. (2015) Crystal structure of tetrawickmanite $Mn^{2+}Sn^{4+}(OH)_6$. Acta Crystallographica, E71, 234-237.

Libowitzsky, E. (1999) Correlation of O-H stretching frequencies and O-H…O hydrogen bond lengths in minerals. Monatschefte für Chemie, 130, 1047-1059.

Mao, H-K., Xu, J. and Bell, P.M. (1986) Calibration of the ruby pressure gauge to 800 kbar under quasi-hydrostatic conditions. Journal of Geophysical Research, 91, 4673-.

Matsui, M., Komatsu, K., Ikeda, E., Sano-Furukawa, A., Gotou, H., and Yagi, T. (2011) The crystal structure of δ-Al(OH)$_3$: Neutron diffraction measurements and ab initio calculations. American Mineralogist, 96, 854-859.

Mitchell, R.H., Welch, M.D. and Chakmouradian, A.R. (2017) Nomenclature of the perovskite supergroup: A hierarchical system of classification based on crystal structure and composition. Mineralogical Magazine 81, 411-461.

Momma, K. and Izumi, F. (2019) VESTA: a Three-Dimensional Visualization System for Electronic and Structural Analysis.

Mookherjee, M., Speziale, S., Marquardt, H., Jahn, S., Wunder, B., Koch-Müller, M. and Liermann, H.-P. Equation of state and elasticity of the 3.65Å phase: Implications for the X-discontinuity. American Mineralogist, 100, 2199-2208.

Najorka, J., Kleppe, A.K. and Welch, M.D. (2019) The effect of pressure and composition on Cu-bearing hydroxide perovskite. Physics and Chemistry of Minerals, 46, 877-887.

Parsons, S.; Pattison, P. and Flack, H.D. (2012) Analysing Friedel averages and differences. Acta Crystallographica, Sect. A68, 736–749.

Pawley, AR., Chinnery, NJ., Clark, SM., and Walter, MJ. (2011). Experimental study of the dehydration of 10Å phase, with implications for its H2O content and stability in subducted lithosphere. Contributions to Mineralogy and Petrology. 162, 1279–1289.

Phillips, B.L., Mason, H.E. and Guggenheim, S. (2007) Hydrogen bonded silanols in the 10Å phase: Evidence from NMR spectroscopy. American Mineralogist 92, 1474–1485.

Rashchenko, S.V., Kamada, S., Hirao, N., Konstantin, D., Litasov, D., and Ohtani, E. (2016) *In situ* X-ray observation of 10Å phase stability at high pressure. American Mineralogist 101, 2564–2569.

Robinson, K., Gibbs, G.V., and Ribbe, P.H. (1971) Quadratic elongation: a quantitative measure of distortion in coordination polyhedra. Science, 172, 567–570.

Ross, N.L., Chaplin, T.D. and Welch, M.D. (2002) Compressibility of stottite, $FeGe(OH)_6$: an octahedral framework with protonated O atoms. American Mineralogist, 87, 1410-1414.

Sclar, C.B., Carrison, L.C., and Schwartz, C.M. (1965) The system $MgO-SiO_2-H_2O$ at high pressures, 25-130 kb and 375-1000°C (extended abstract), Basic Science Division, American Ceramic society Fall Meeting, Paper 2-b-65-F.

Syracuse, E.M., van Keken, P.E., and Abers, G.A. (2010) The global range of subduction zone thermal models. Physics of the Earth and Planetary Interiors, 183, 73-90.

Welch, M.D. and Crichton, W.A. (2002) Compressibility to 7 GPa at 298K of the protonated octahedral framework mineral burtite, $CaSn(OH)_6$. Mineralogical Magazine, 66, 431-440.

Welch, M.D. and Kleppe, A.K. (2016) Polymorphism of the hydroxide perovskite $Ga(OH)_3$ and possible proton-driven transformational behaviour. Physics and Chemistry of Minerals, 43, 515-526.

Welch, M.D., Pawley, A.R., Ashbrook, S.E., Mason, H.E. and Phillips, B.L. (2006) Si vacancies in the 10- Å phase. American Mineralogist, 91, 1707-1710.

Welch, M.D. and Wunder, B. (2012) A single-crystal X-ray diffraction study of the 3.65 Å phase MgSi(OH)$_6$, a high-pressure hydroxide perovskite. Physics and Chemistry of Minerals, 39, 693-697.

Wunder, B., Wirth, R. and Koch-Muller, M. (2011) The 3.65Å phase in the system MgO-SiO$_2$-H$_2$O: Synthesis, composition, and structure. American Mineralogist, 96, 1207-1214.

Wunder, B., Jahn, S., Koch-Müller, M. and Speziale, S. (2012) The 3.65Å phase, MgSi(OH)$_6$: Structural insights from DFT calculations and T-dependent IR spectroscopy American Mineralogist, 97, 1043-1048.

FIGURE CAPTIONS

Figure 1. The polyhedral topology of MgSi(OH)$_6$ consists of a framework of highly rotated, corner-sharing, alternating MgO$_6$ (yellow) and SiO$_6$ (blue) octahedra. All oxygen atoms form OH groups. H atoms are shown as small pink spheres. **(a)** View of the framework along the b axis projected onto (010) in which a single ..O-H…O-H…O-H.. crankshaft extending parallel to [001] is highlighted as a crooked red line. **(b)** View of the structure along the c axis projected onto (001) and showing a single ..O-H…O-H…O-H.. zigzag chain as a green line extending parallel to [010]. Crankshafts are shown end-on as pink blocks.

Figure 2. DEPOSITED ITEM. Output from a SHELX.LST file for three stages of refinement of the $P2_1$ structure before H atoms are included in the model. Highlighted in yellow are peaks in unmodelled residual electron density that correspond to H atoms. The header of each block of entries gives some details of the stage of refinement and associated agreement

indices. All ten H atoms of the $P2_1$ structure appear in the difference-Fourier map after only 5 cycles of isotropic least-squares refinement. The penultimate column gives values of the electron density (e/Å^3) which closely approximate to the number of electrons at this site. The last column gives the distance to and identity of the first-nearest-neighbor atom. The first two rows of each block correspond to the two fully-occupied H sites of the two zig-zag chains. The remaining eight highlighted peaks correspond to the half-occupied crankshaft H sites. See text for further explanation.

Figure 3. Crankshaft topologies of $P2_1/n$ and $P2_1$ structures determined in this study and the $P2_1$ crankshaft modeled using Density Functional Theory by Wunder et al. (2012). The experimentally determined structures are shown with half-occupied H sites, whereas the DFT model is shown with four fully occupied non-equivalent H sites. Values of O…O distances of the $P2_1$ crankshaft shown in black and green are for 100 K and 293 K, respectively.

Note that O_D…O_A distances for the DFT crankshaft are much shorter than those determined experimentally.

Figure 4. (a) Variation of the normalised unit cell parameters with pressure for crystal 6. Blue = a, red = b, green = c. The dashed lines are fits to 2nd-order Birch-Murnaghan equation of states. Circles with a central dot are data collected on decompression. The derived axial moduli are $K_{a0} = 68.2(8)$ GPa, $K_{b0} = 85.1(9)$ GPa, $K_{c0} = 89.4(7)$ GPa (K' fixed at 4 for all). **(b)** Variation of the normalised unit cell volume with pressure shown fitted to a 2nd-order Birch-Murnaghan equation of state for which the derived bulk modulus is $K_0 = 80.3(9)$ GPa (K' fixed at 4).

Figure 5. Graphics showing the shapes and relative sizes of atom displacement ellipsoids for anisotropic refinements of the $P2_1/n$ structure for ambient out-of-cell and 6.2 GPa data. The comparison illustrates the similarity of the shapes and sizes of the ellipsoids for the two experiments and supports the proposition that the absorption was very well modelled for high-pressure datasets. The shape and size of anisotropic displacement ellipsoids are very sensitive to the quality of an absorption correction. A poor correction will be manifested in highly distorted and often extremely elongated ellipsoids.

Figure 6. Variations in Mg-O and Si-O bond lengths with pressure for crystal 6. (a, c) $P2_1/n$; (b,d) $P2_1$. Circles with a central dot are data collected on decompression. See text for discussion.

Figure 7. Variations in $O_D….O_A$ distances. Symbols are for the $P2_1$ structure and the associated dotted black lines show trends of values for the $P2_1/n$ structure. Circles with a central dot are data collected on decompression. The two longest distances correspond to the zig-zag chains of the $P2_1$ structure, the four much shorter distances of relate to the crankshaft. To a good approximation the trends for the $P2_1/n$ structure mirror those of the $P2_1$ structure. See text for discussion.

Figure 8. Variations in Mg-O-Si angles of the $P2_1$ structure (symbols) and $P2_1/n$ structure (dashed lines) with pressure. Circles with a central dot are data collected on decompression. All trends vary smoothly without any obvious discontinuities.

Figure 9. Variations with pressure of the volumes of **(a)** SiO_6 and **(b)** MgO_6 octahedra for the $P2_1/n$ (red triangles) and $P2_1$ (inverted blue triangles) structures. The values for both structures are essentially the same. See text for discussion.

TABLE CAPTIONS

Table 1. Summary of the results for the refinement of the 100 K structure of $MgSi(OH)_6$ crystal 7 for space group $P2_1$.

Table 2. Atom coordinates and atom displacement parameters U_{ij} (Å^2) of $MgSi(OH)_6$ crystal 7 at 100 K for refinements for space groups $P2_1/n$ and $P2_1$. *Overall displacement parameter refined for H atoms. ** H atoms of the zigzag chains.

Table 3. Bond lengths and polyhedral parameters for $MgSi(OH)_6$ crystal 7 at 100 K for space groups $P2_1/n$ and $P2_1$.

Table 4. Unit cell parameters of $MgSi(OH)_6$ crystal 6 at various pressures.

Table 5. Summary of refinements of the structure of $MgSi(OH)_6$ crystal 6 for space groups $P2_1/n$ and $P2_1$ at various pressures. Upper entry is $P2_1/n$ and lower entry is $P2_1$.

Table 6. Oxygen donor-acceptor distances of $MgSi(OH)_6$ crystal 6 for space groups $P2_1/n$ and $P2_1$ at various pressures.

Table 7. Polyhedral parameters of $MgSi(OH)_6$ crystal 6 for space groups $P2_1/n$ and $P2_1$ before and after high-pressure experiment.

	$P2_1$								$P2_1/n$		
	Mg-O (Å)				Si-O(Å)					Mg-O (Å)	Si-O(Å)
	100K		293K		100K		293K			100K aniso	
	iso	aniso	aniso		iso	aniso	aniso		O1	2.1229(8)	1.7788(8)
O1	2.072(3)	2.070(3)	2.078(3)	O1	1.792(3)	1.792(3)	1.790(3)		O2	2.0763(8)	1.7881(8)
O2	2.082(3)	2.084(3)	2.084(3)	O2	1.784(3)	1.784(3)	1.787(3)		O3	2.0696(8)	1.8087(8)
O3	2.084(5)	2.083(6)	2.086(6)	O3	1.797(3)	1.795(3)	1.796(3)		average	2.090	1.792
O4	2.115(4)	2.116(4)	2.121(4)	O4	1.782(4)	1.786(5)	1.782(5)				
O5	2.054(5)	2.055(6)	2.062(6)	O5	1.822(3)	1.823(3)	1.823(3)		$V(Å^3)$	12.15	7.67
O6	2.131(4)	2.130(4)	2.132(4)	O6	1.776(4)	1.773(5)	1.779(5)		$DI*$	0.0107	0.0064
average	2.090	2.090	2.094	average	1.792	1.792	1.793		$\sigma*$	1.001	1.000
									$\lambda*$	2.34	0.53
$V(Å^3)$	12.15	12.15	12.22	$V(Å^3)$	7.67	7.67	7.68				
$DI*$	0.0106	0.0107	0.0105	$DI*$	0.0066	0.0063	0.0061				
$\sigma*$	1.001	1.001	1.001	$\sigma*$	0.983	0.989	1.000				
$\lambda*$	2.79	2.82	2.83	$\lambda*$	1.0004	1.0004	0.965				

* After Robinson et al. (1971).

	$P2_1$					
	O1…O1	O2…O2	O3…O5	O4…O5	O3…O6	O4…O6
100 K						
$d(O_D…O_A)$ (Å)	2.946(4)	2.939(2)	2.768(3)	2.772(3)	2.813(3)	2.720(2)
∠O-H…O (°)	169(4)	159(4)	153(7), 169(7)	155(8), 166(7)	164(7), 170(8)	163(6), 163(7)
293 K						
$d(O_D…O_A)$ (Å)	2.957(4)	2.951(2)	2.780(3)	2.789(4)	2.820(3)	2.731(3)
∠O-H…O (°)	165(4)	164(4)	161(7), 164(7)	168(7), 171(11)	173(7), 173(8)	159(7), 168(8)

TABLE 4

P (GPa)	a (Å)	b (Å)	c (Å)	β	V (Å³)
0.0001[b]	5.1111(1)	5.1872(1)	7.3272(1)	90.032(2)	194.261(6)
0.0001[a]	5.1119(1)	5.1885(1)	7.3283(2)	90.037(2)	194.366(8)
0.71(6)	5.090(1)	5.1723(6)	7.3049(4)	90.042(7)	192.32(5)
2.76(14)	5.045(1)	5.1337(5)	7.2550(3)	90.047(6)	187.90(4)
3.53(3)*	5.028(1)	5.1186(8)	7.2324(5)	90.02(1)	186.15(6)
4.73(12)	5.003(1)	5.0966(6)	7.2045(3)	90.014(7)	183.72(5)
4.84(3)*	5.005(1)	5.1005(7)	7.2081(5)	90.029(9)	184.01(6)
6.22(4)	4.983(1)	5.0795(6)	7.1812(3)	90.034(8)	181.76(5)
7.23(3)	4.961(1)	5.0633(5)	7.1579(3)	89.987(8)	179.79(5)
8.40(5)	4.945(1)	5.0455(5)	7.1372(3)	90.009(8)	178.06(5)
9.11(1)	4.933(2)	5.0345(8)	7.1213(5)	90.03(1)	176.86(6)

b = out-of-cell ambient before high-pressure experiment.

a = out-of-cell ambient after high-pressure experiment.

*collected on decompression.

TABLE 5

P (GPa)	$I_{collected}$	R_{int}	$I>2\sigma(I)$	I(total)	R_1 (all)	wR_2 (all)	GoF	$\rho(e^-/Å^3)$ max, min
0.0001[b]	5525	0.023	826	902	0.029	0.065	1.377	0.35, -0.26
	5769	0.021	1787	1555	0.034	0.073	1.050	0.56, -0.50
0.0001[a]	5446	0.029	835	911	0.031	0.064	1.344	0.44, -0.29
	5684	0.029	1799	1539	0.044	0.107	1.115	0.98, -0.66
0.71(6)	2249	0.035	215	240	0.050	0.124	1.187	0.48, -0.42
	2356	0.035	373	425	0.055	0.158	1.243	0.54, -0.58
2.76(14)	2229	0.032	207	235	0.052	0.125	1.132	0.55, 0.41
	2345	0.032	357	414	0.051	0.129	1.154	0.51, -0.44
3.53(3)*	2295	0.035	213	240	0.051	0.129	1.109	0.47, -0.53
	2440	0.034	368	427	0.052	0.131	1.094	0.46, -0.52
4.73(12)	2173	0.033	214	230	0.049	0.129	1.146	0.45, -0.39
	2316	0.032	369	412	0.056	0.174	1.131	0.73, -0.80
4.84(3)*	2213	0.033	207	233	0.055	0.138	1.207	0.51, -0.47
	2376	0.032	354	409	0.054	0.137	1.128	0.51, -0.47
6.22(4)	2157	0.030	210	233	0.051	0.133	1.118	0.50, -0.49
	2275	0.029	358	406	0.049	0.134	1.131	0.46, -0.49
7.23(3)	2167	0.038	204	228	0.048	0.128	1.187	0.40, -0.47
	2279	0.036	356	400	0.047	0.124	1.110	0.42, -0.54
8.40(5)	2188	0.036	204	226	0.048	0.129	1.175	0.46, -0.40
	2313	0.035	349	397	0.050	0.129	1.123	0.40, -0.45
9.11(1)	2054	0.037	195	218	0.053	0.145	1.139	0.55, -0.53
-	-	-	-	-	-	-	-	-

b = out-of-cell ambient before high-pressure experiment.

a = out-of-cell ambient after high-pressure experiment.

* collected on decompression.

TABLE 6

	$P2_1/n$					$P2_1$					
P (GPa)	O1...O1	O2...O2	O3...O3	O1...O3	P (GPa)	O1…O1	O2…O2	O3…O5	O4…O5	O3…O6	O4…O6
0^b	2.777(2)	2.952(1)	2.731(1)	2.801(1)	0^b	2.949(2)	2.955(2)	2.777(2)	2.787(3)	2.815(3)	2.730(2)
0^a	2.778(2)	2.953(1)	2.731(2)	2.802(1)	0^a	2.949(4)	2.954(4)	2.780(4)	2.783(4)	2.816(4)	2.730(4)
0.71(6)	2.759(6)	2.939(4)	2.719(5)	2.785(4)	0.71(6)	2.94(1)	2.94(1)	2.72(1)	2.763(9)	2.812(9)	2.77(2)
2.76(1)	2.722(6)	2.904(4)	2.679(5)	2.745(3)	2.76(1)	2.915(8)	2.90(1)	2.68(1)	2.730(7)	2.756(6)	2.72(1)
3.53(3)*	2.714(8)	2.886(4)	2.661(6)	2.728(4)	3.53(3)*	2.87(1)	2.902(9)	2.66(1)	2.705(7)	2.748(7)	2.72(1)
4.73(1)	2.698(6)	2.868(4)	2.653(5)	2.702(4)	4.73(1)	2.884(9)	2.862(7)	2.65(1)	2.685(7)	2.720(6)	2.70(1)
4.84(3)*	2.695(7)	2.871(5)	2.648(6)	2.705(4)	4.84(3)*	2.86(1)	2.88(1)	2.65(1)	2.679(7)	2.726(7)	2.70(1)
6.22(4)	2.679(7)	2.849(4)	2.630(6)	2.683(4)	6.22(4)	2.856(7)	2.850(8)	2.63(1)	2.662(6)	2.699(6)	2.68(1)
7.23(3)	2.663(7)	2.837(4)	2.618(6)	2.665(4)	7.23(3)	2.912(7)	2.787(6)	2.61(1)	2.677(5)	2.657(6)	2.66(1)
8.40(5)	2.650(7)	2.823(4)	2.601(6)	2.648(4)	8.40(5)	2.896(9)	2.772(7)	2.60(1)	2.661(7)	2.638(8)	2.65(1)
9.11(1)	2.642(9)	2.814(5)	2.592(7)	2.639(4)							

b = out-of-cell ambient before high-pressure experiment.

a = out-of-cell ambient after high-pressure experiment.

* collected on decompression.

TABLE 7

P2₁/n

	Mg-O (Å)			Si-O (Å)	
	before	after		before	after
$O1^{x2}$	2.0723(8)	2.0732(8)	$O1^{x2}$	1.8098(8)	1.8095(8)
$O2^{x2}$	2.0799(8)	2.0794(8)	$O2^{x2}$	1.7873(8)	1.7873(8)
$O3^{x2}$	2.1265(8)	2.1269(8)	$O3^{x2}$	1.7794(8)	1.7796(8)
average	2.093	2.093	average	1.792	1.792
$V(Å^3)$	12.209	12.214	$V(Å^3)$	7.673	7.676
*DI**	0.0107	0.0108	*DI*	0.0066	0.0064
σ*	2.23	2.23	σ	0.51	0.49
λ*	1.0009	1.0009	λ	1.0002	1.0002

P2₁

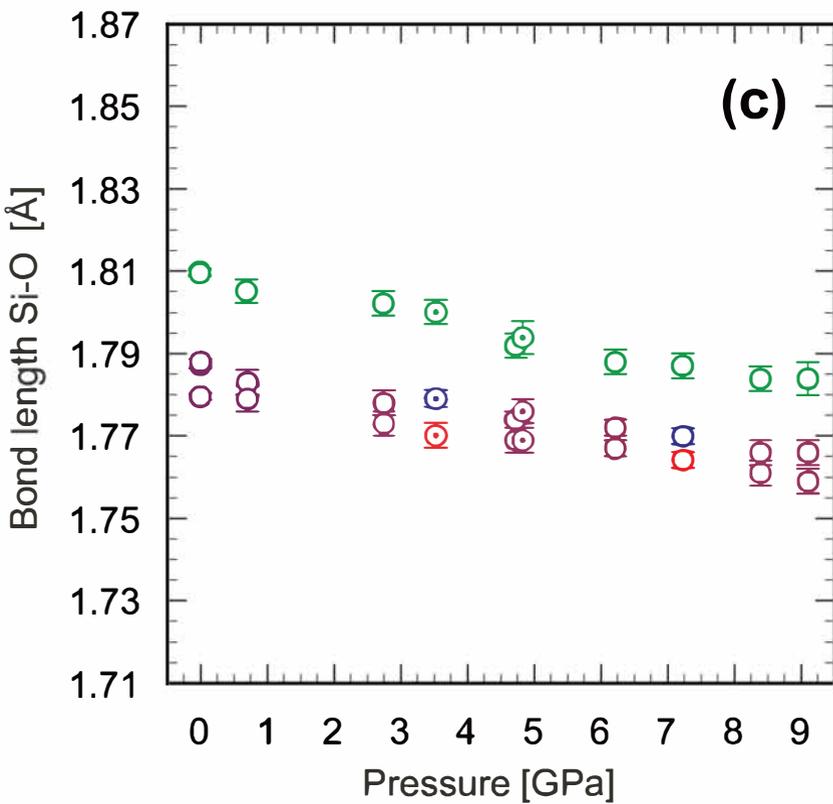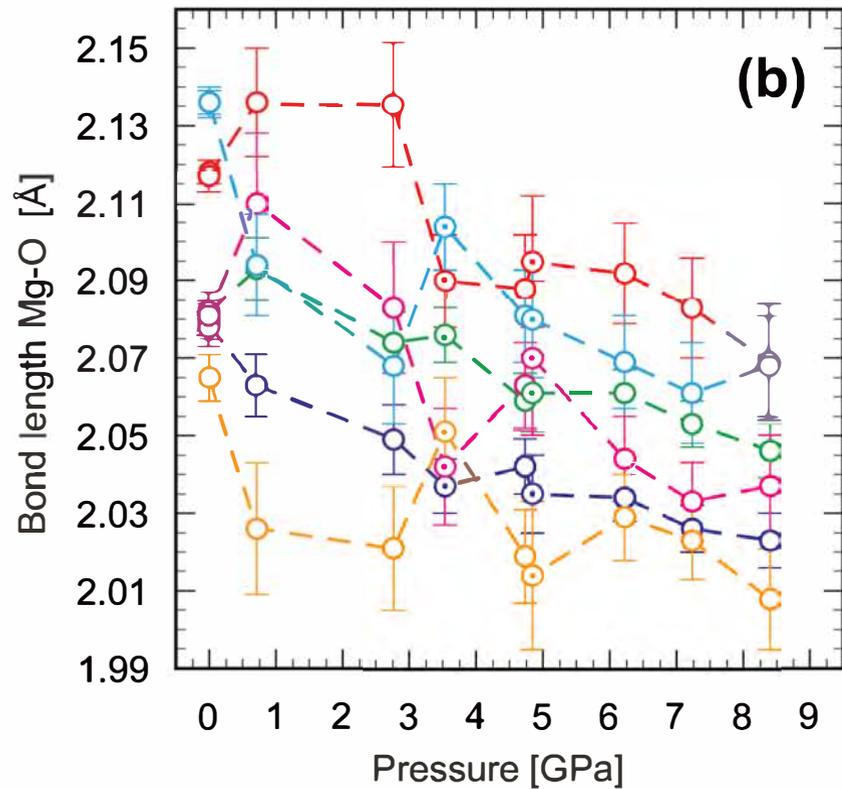|	Mg-O (Å)			Si-O(Å)	
	before	after		before	after
O1	2.082(3)	2.078(3)	O1	1.786(3)	1.791(3)
O2	2.079(3)	2.078(3)	O2	1.788(3)	1.786(3)
O3	2.081(5)	2.086(6)	O3	1.802(3)	1.802(3)
O4	2.117(3)	2.119(4)	O4	1.783(4)	1.785(5)
O5	2.062(5)	2.061(6)	O5	1.820(3)	1.818(3)
O6	2.135(3)	2.135(4)	O6	1.777(4)	1.777(5)
average	2.093	2.094	average	1.793	1.793
$V(Å^3)$	12.20	12.22	$V(Å^3)$	7.68	7.68
*DI**	0.0107	0.0107	*DI*	0.0068	0.0062
σ*	1.001	1.001	σ	1.000	1.000
λ*	2.65	2.77	λ	0.95	0.92
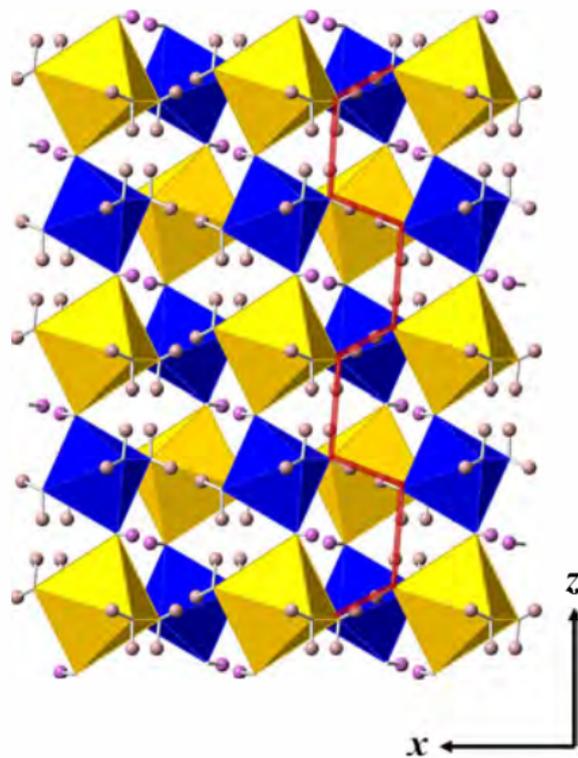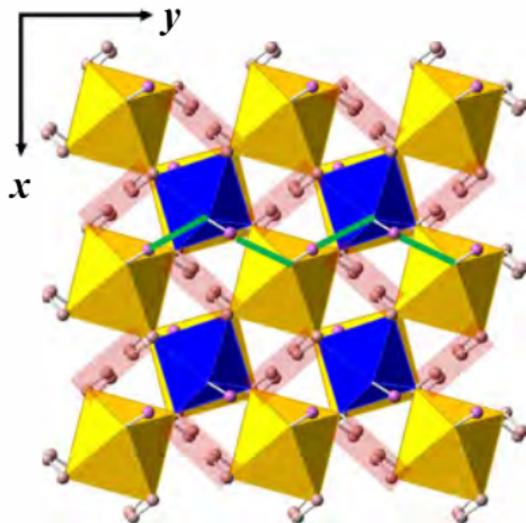
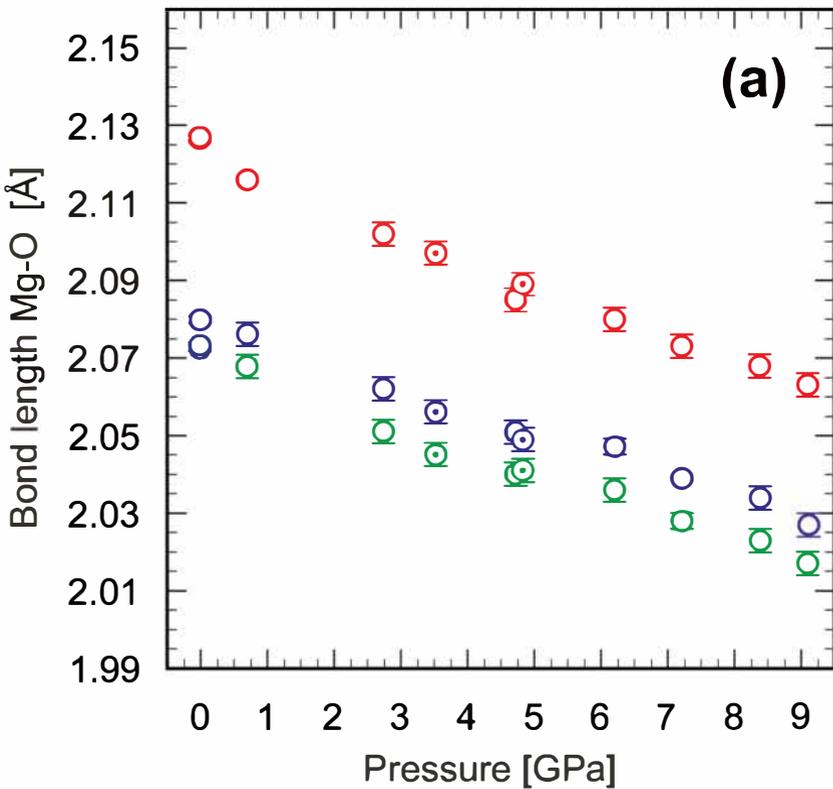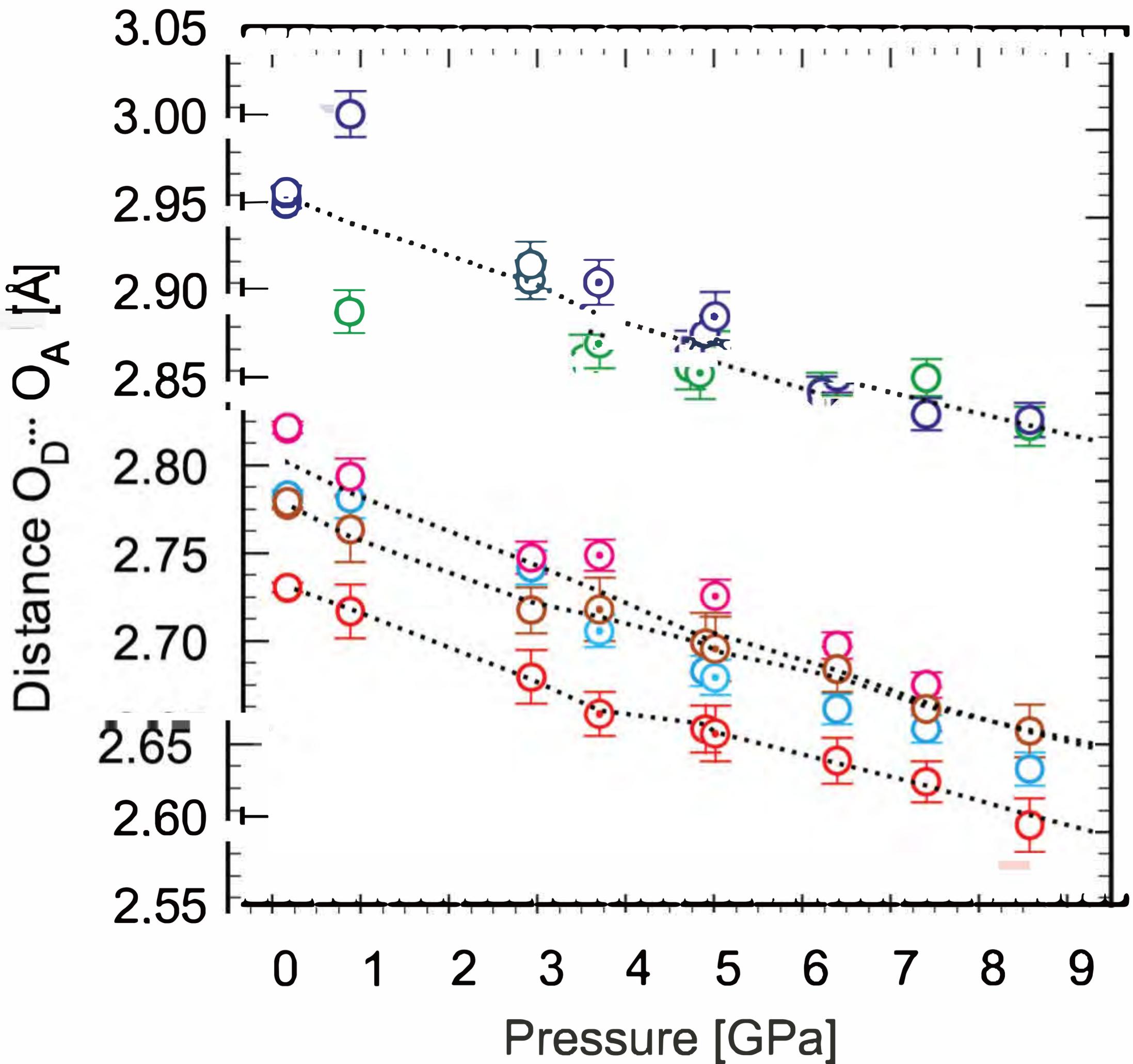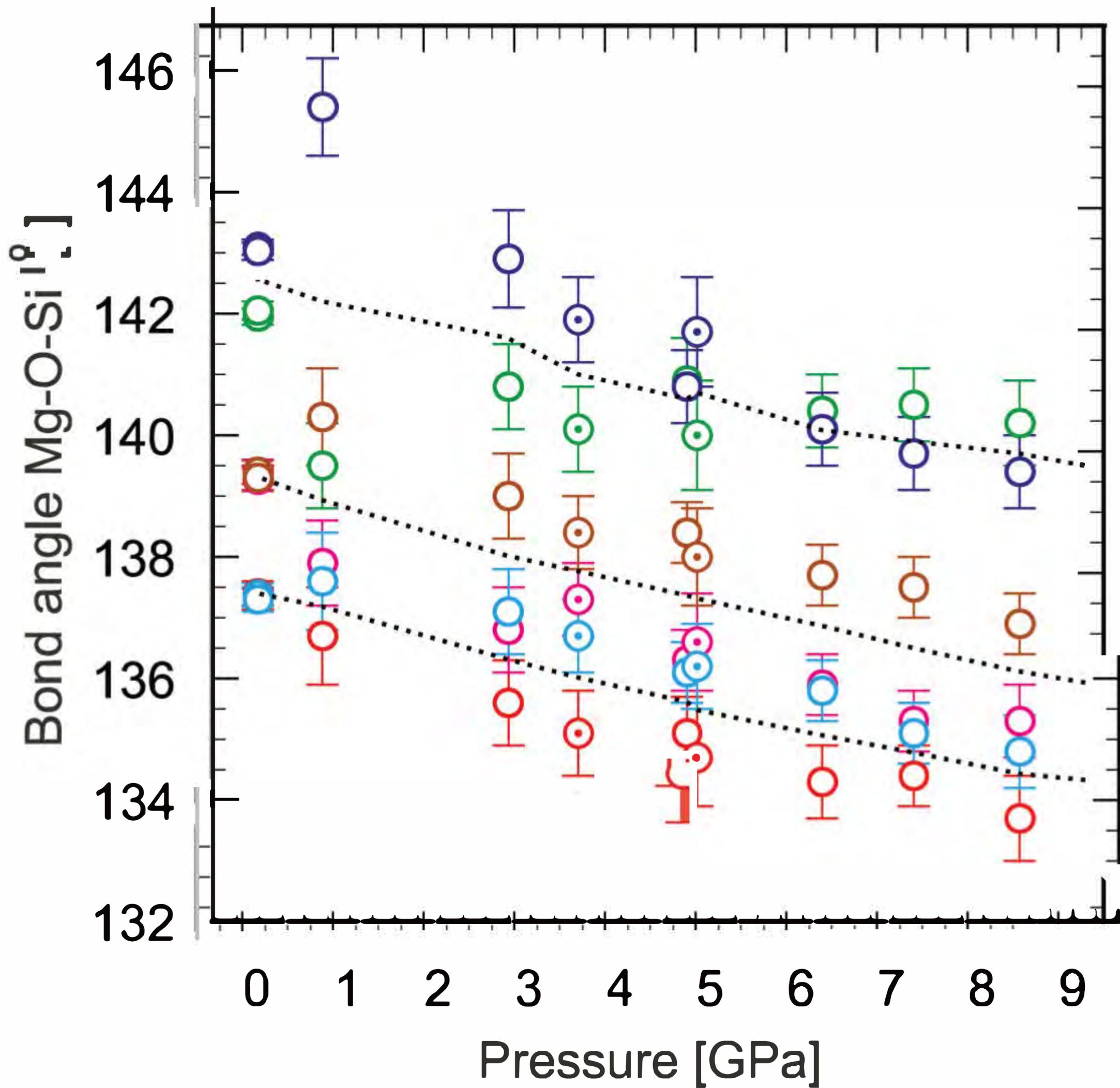**FIGURE 1**

a　　　　**b**

FIGURE 3
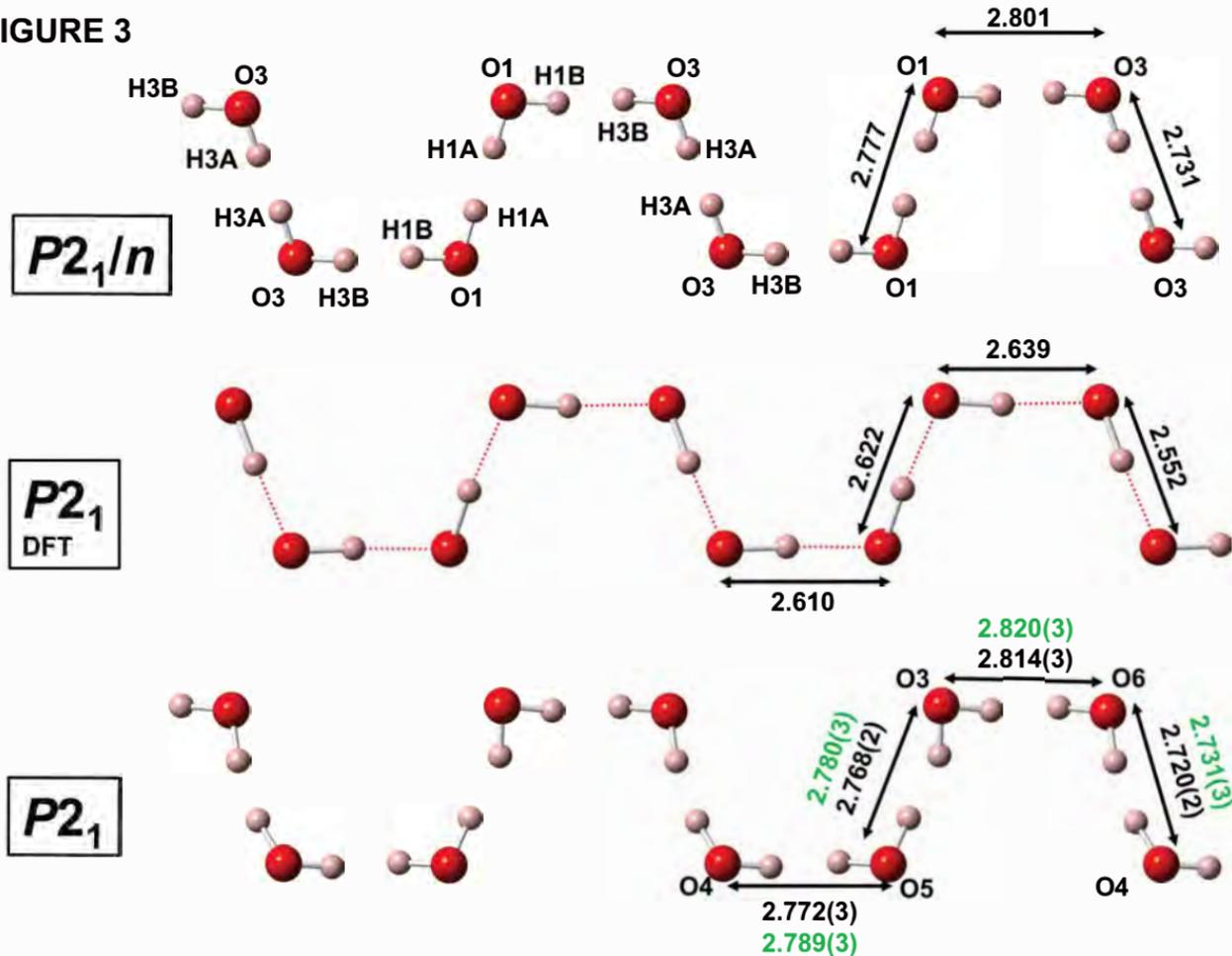
FIGURE 4
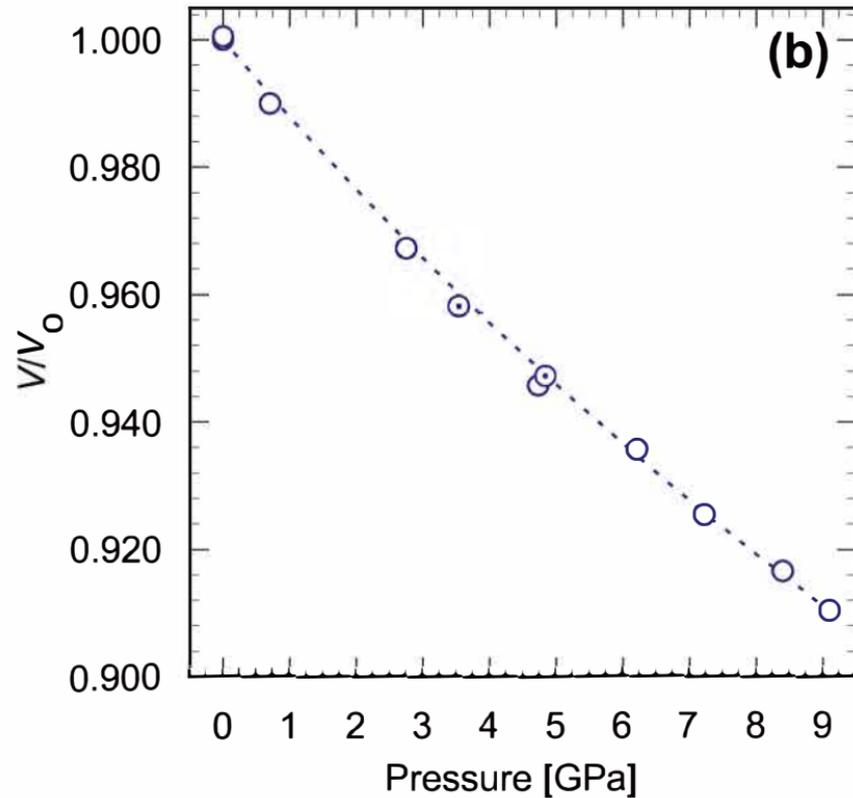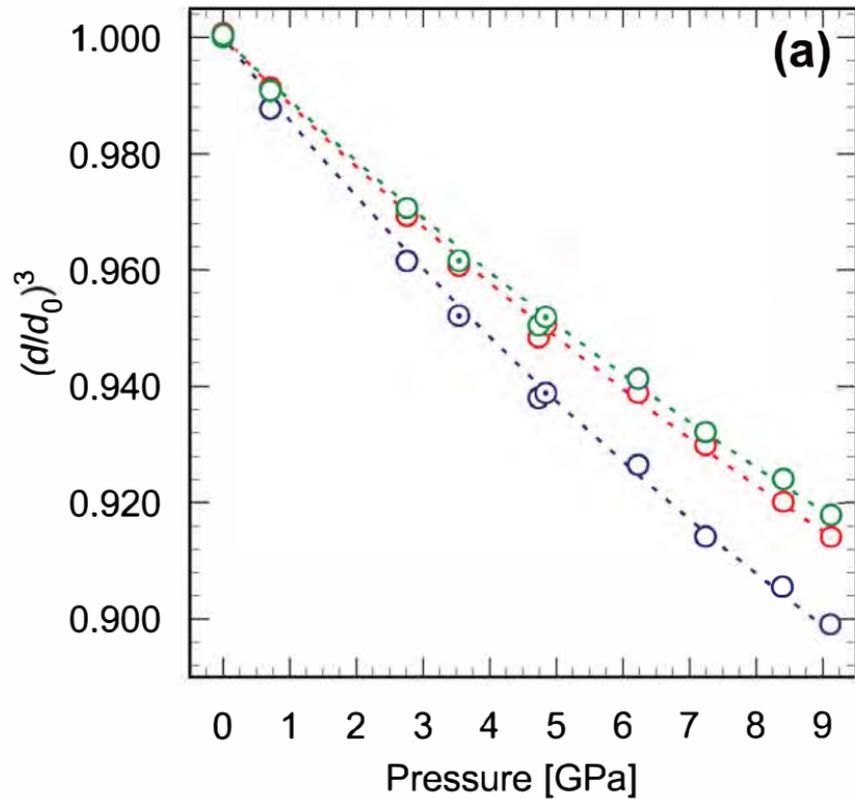
FIGURE 5
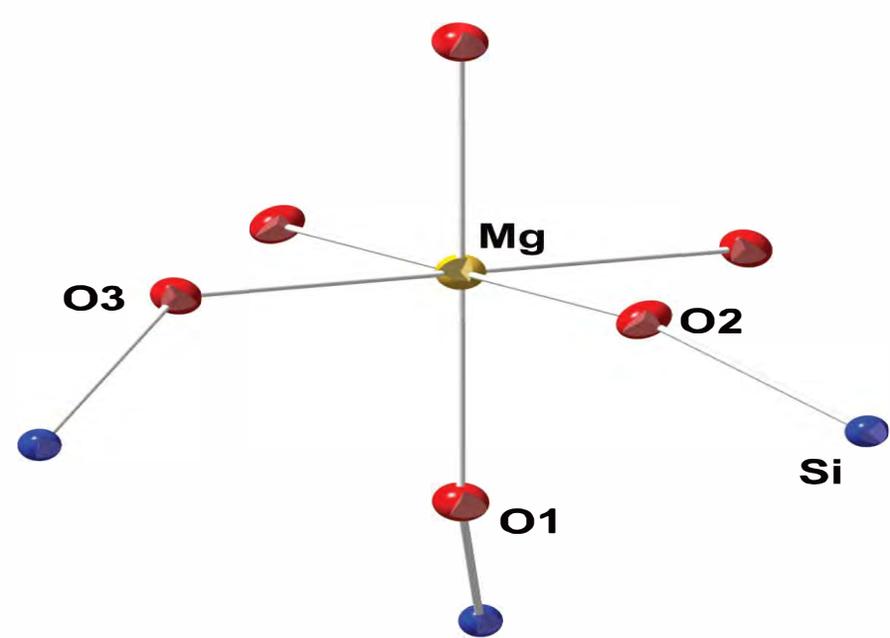
ambient out-of-cell
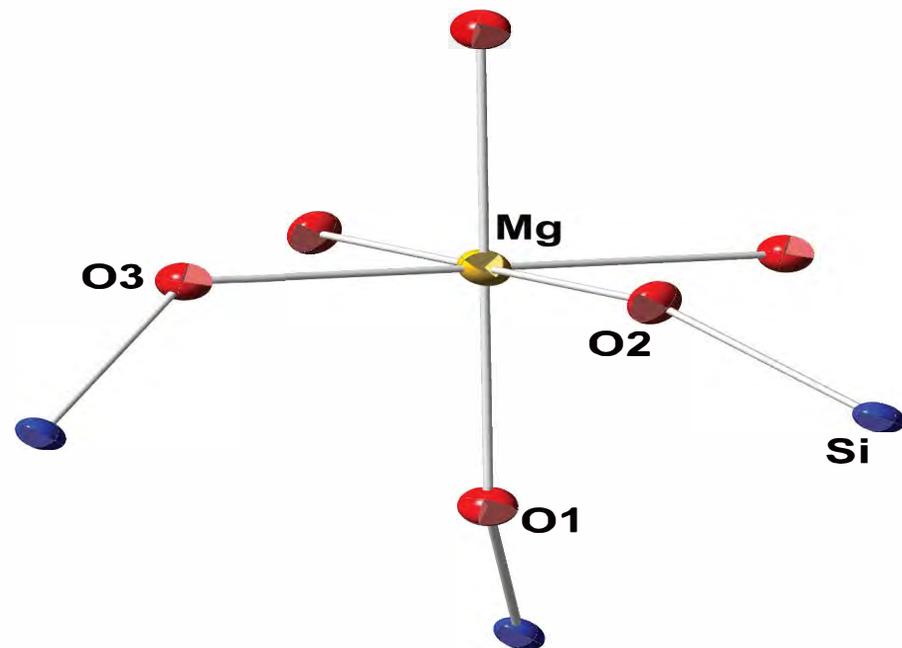
6.2 GPa
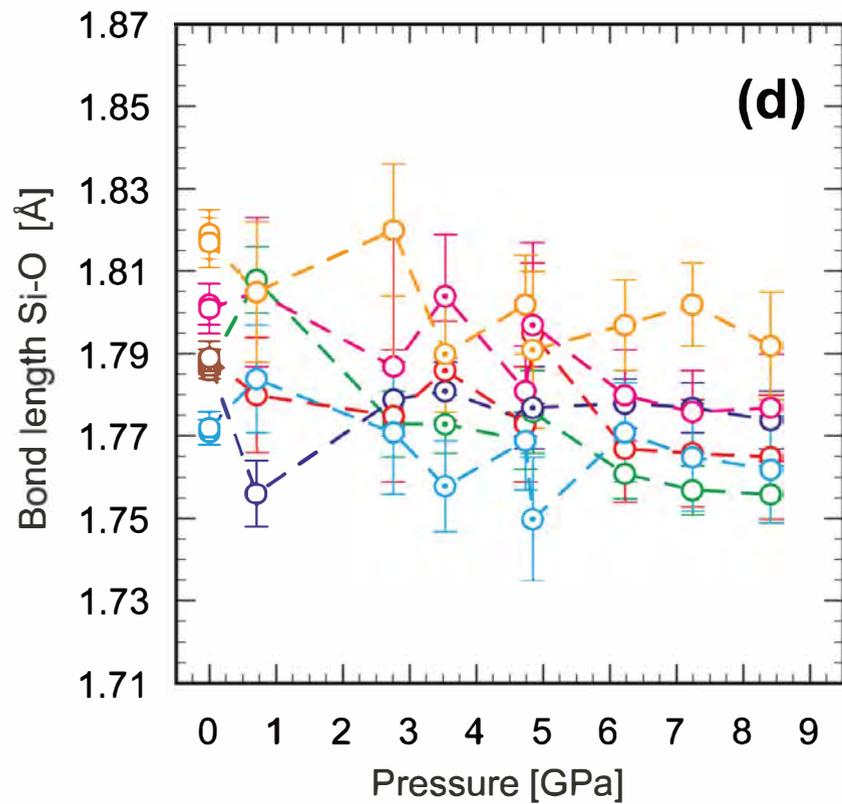
FIGURE 7

FIGURE 8

FIGURE 9